Supplementary Information

A Sequential Doping Strategy for Architecturally Controlled $BiVO_4$ Photoanodes with Synergistic Co-Doping Enabled by BiOI Conversion

Shubham Kumar, and Suddhasatwa Basu*

Department of Chemical Engineering, Indian Institute of Technology Delhi, New Delhi 110016, India.

*E-mail: sbasu@iitd.ac.in

Materials: Bismuth(III) nitrate pentahydrate ($Bi(NO_3)_3{\cdot}5H_2O$, 98%), sodium iodide (NaI, 99.5%), p-benzoquinone ($C_6H_4O_2$, ≥98%), vanadium(IV)-oxy acetylacetonate ($VO(acac)_2$, 98%), and niobium(V) chloride ($NbCl_5$, 99.5%) were purchased from Sigma-Aldrich. Acetone (C_3H_6O) and isopropyl alcohol ($(CH_3)_2CHOH$), dipotassium hydrogen phosphate anhydrous (K_2HPO_4, 98%), and potassium dihydrogen phosphate anhydrous (KH_2PO_4, 99%), were purchased from Fisher Scientific. Dimethyl sulfoxide ($(CH_3)_2SO$, 99.8%), sodium hydroxide (NaOH, 98%), Barium chloride dihydrate ($BaCl_2{\cdot}2H_2O$), nickel(II) chloride hexahydrate ($NiCl_2{\cdot}6H_2O$, 98%), and iron(III) chloride hexahydrate ($FeCl_3{\cdot}6H_2O$, 98%) were procured from Sisco Research Laboratories (SRL). Absolute ethanol (C_2H_5OH) was received from Merck. Fluorine-doped tin oxide (FTO) coated glass substrates (sheet resistance ~14 Ω/sq) were supplied by Macwin, India. Deionized (DI) water with a resistivity of 18.2 MΩ·cm, used in all experiments, was prepared using a RIONS LABPURE water solutions system.

Calculation of Film Mass and Dopant Precursor Quantities. The theoretical mass of the deposited film was quantified based on the total charge density passed during the electrodeposition of the BiOI precursor, measured at 0.16 C/cm². According to Faraday's Law ($n = Q/zF$, with $z = 2$), the charge produced 8.29×10^{-7} moles of BiOI. Following a complete 1:1 molar conversion to $BiVO_4$, the final mass of the pure photoactive film was calculated to be 0.268 mg.

To achieve a target doping concentration of 0.1 atomic % for both Niobium (Nb) and Barium (Ba), the required molar amount for each dopant was determined to be 8.29×10^{-10} mol. For accurate and reproducible incorporation, working solutions of the precursors ($NbCl_5$ and $BaCl_2 \cdot 2H_2O$) in dimethyl sulfoxide (DMSO) were prepared via serial dilution from 10 mM stock solutions. The final concentration of these working solutions was maintained at 8.29 µM, enabling the delivery of a precise molar quantity in a volume of 100 µL. This volume of each

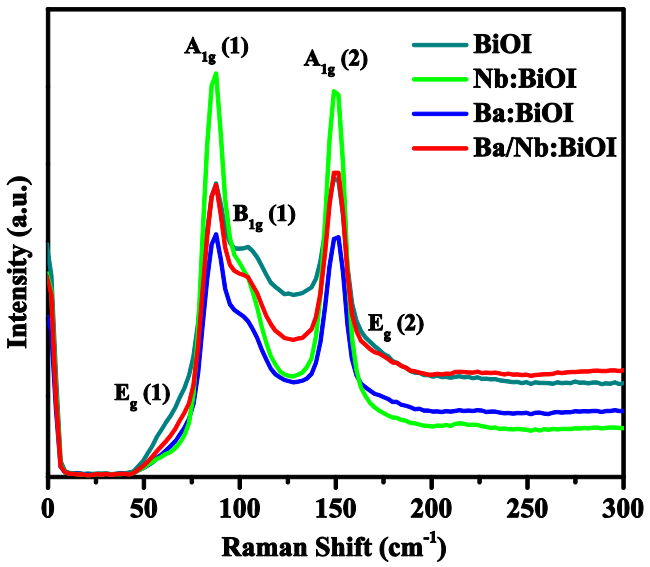

Fig. S1. Raman spectra of deposited BiOI at the intermediate step after heating at 200˚C at Room temperature.

dopant solution was added to the BiOI film following the sequential method described in the manuscript.

Raman Study of BiOI film. The Raman spectra of pristine BiOI film and its modified samples (Nb–BiOI, Ba–BiOI, and Nb/Ba–BiOI) reveal distinct lattice responses to elemental modification, shown in Fig. S1. Pristine BiOI exhibits the characteristic $E_g(1)$ (~58 cm^{-1}), $A_{1g}(1)$ (~88 cm^{-1}), $B_{1g}(1)$ (~105 cm^{-1}), and $A_{1g}(2)$ (~150 cm^{-1}) modes, corresponding to in-plane vibrations, out-of-plane Bi–I stretching, O–Bi–O bending, and Bi–O stretching. In Nb–BiOI, the $E_g(1)$ mode red-shifts to ~56 cm^{-1} with decreased intensity, while the $A_{1g}(1)$ peak sharpens and dominates the spectrum, and the $B_{1g}(1)$ feature weakens, which signifies lattice relaxation, oxygen-vacancy formation, and enhanced out-of-plane order due to partial BiO_{2-x} formation. In contrast, Ba–BiOI shows an overall decrease in Raman intensity without frequency shifts, indicating that Ba predominantly forms a surface $BaCl_2 \cdot xH_2O$ layer with minimal lattice distortion. Upon sequential modification, the Nb/Ba–BiOI film exhibits Raman features that approach those of pristine BiOI, with partial recovery of A_{1g} and B_{1g} symmetry and an intermediate E_g intensity. By correlating XRD and Raman analyses, we infer that Nb induces structural distortion and oxygen-vacancy disorder through BiO_{2-x} formation, whereas Ba segregates on the surface as $BaCl_2 \cdot xH_2O$ and, in sequential modification, partially compensates Nb-induced lattice distortions and oxygen-vacancy disorder near the film surface, thereby improving lattice coherence while preserving a controlled defect concentration.

Table S1. Unit cell volume and parameters of prepared photoanodes.

Parameters	BVO	Nb-BVO	Ba-BVO	Nb/Ba-BVO
a (Å)	5.191(3)	5.193(1)	5.192(3)	5.194(2)

b (Å)	5.099(3)	5.103(1)	5.101(3)	5.102(2)
c (Å)	11.704(6)	11.708(2)	11.707(5)	11.711(3)
V (Å^3)	309.79(3)	310.13(2)	309.99(3)	310.32(2)

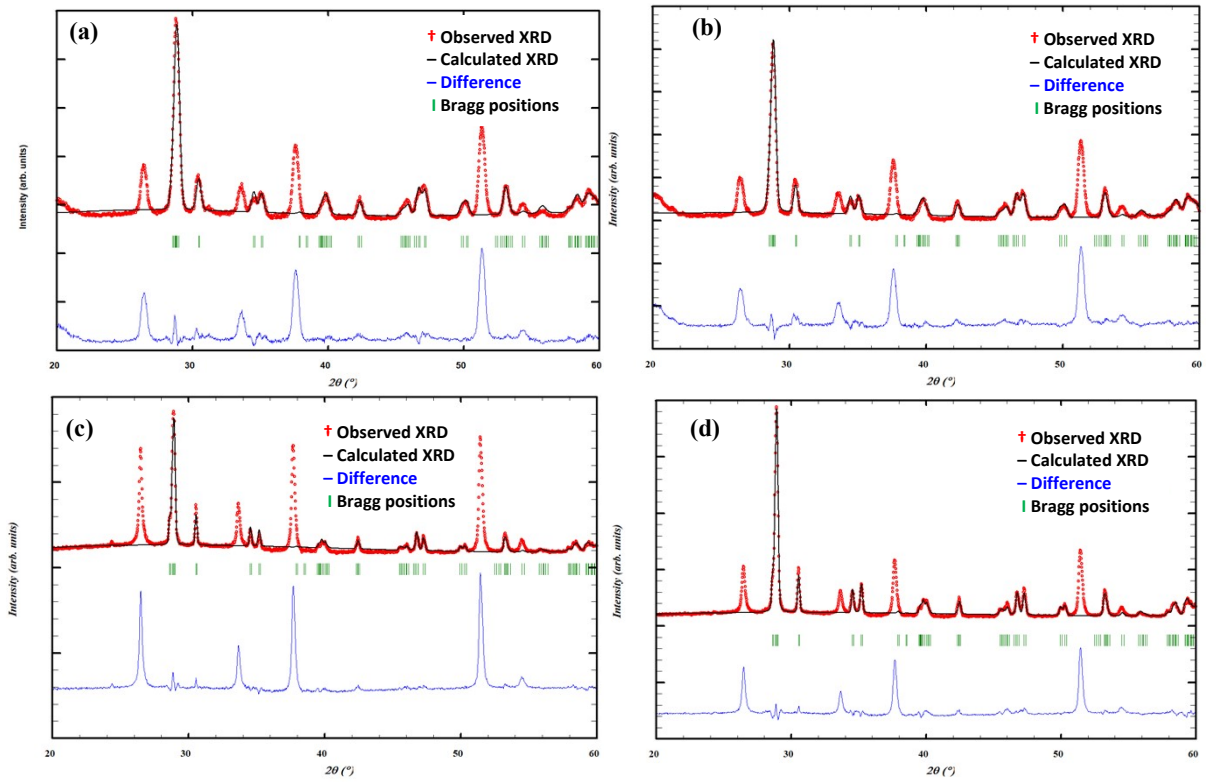

Fig. S2. Rietveld refinement profile of XRD data for (a) pristine BiVO4, (b) Nb-BiVO4, (c) Ba-BiVO4, and (d) Nb/Ba-BiVO4. Observed (+), calculated (–), and difference (bottom) profiles are shown. The vertical bars represent the Bragg positions.

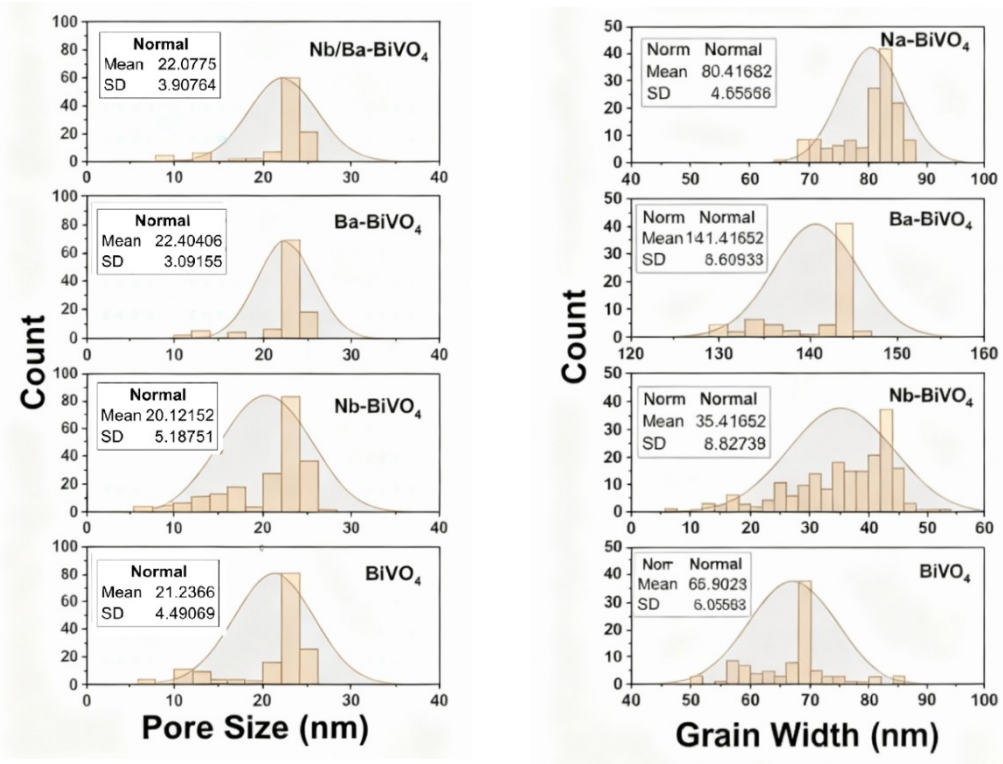

Fig. S3. (a) Pore Size and (b) Grain Width of $BiVO_4$, Nb-$BiVO_4$, Ba-$BiVO_4$, and Nb/Ba-$BiVO_4$ based on SEM image.

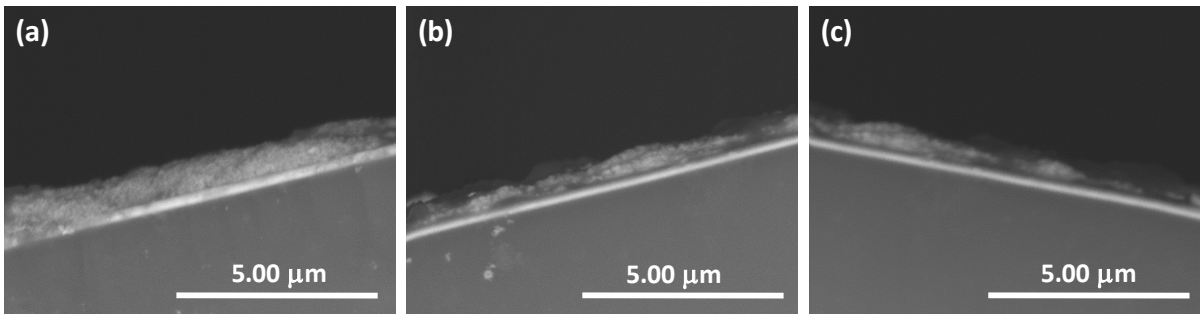

Fig. S4. Cross sectional SEM image for film thickness comparison of Nb-$BiVO_4$, Ba-$BiVO_4$, and Nb/Ba-$BiVO_4$.

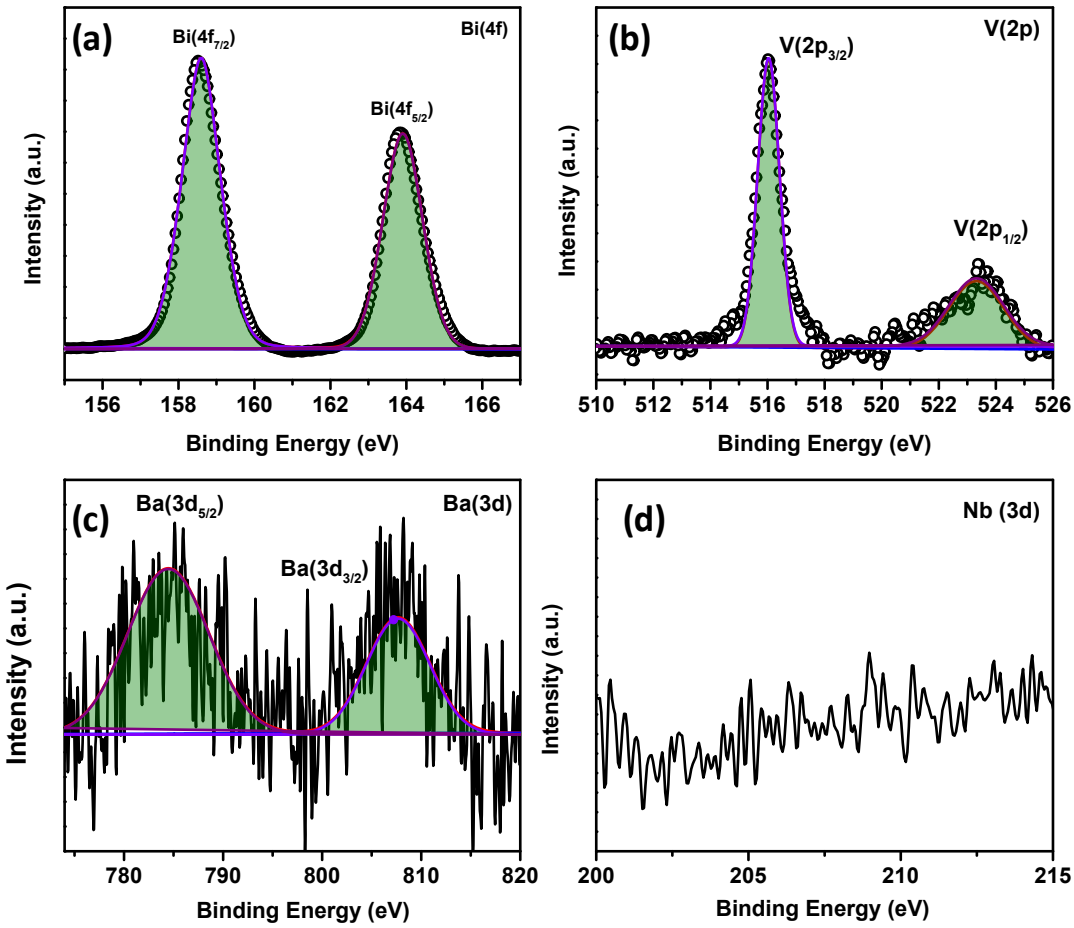

Fig. S5. XPS of Nb/Ba-BiVO4 film; High resolution XPS spectrum of (a) Bi4f, (b) V2p, (c) Ba3d and (d) Nb3d

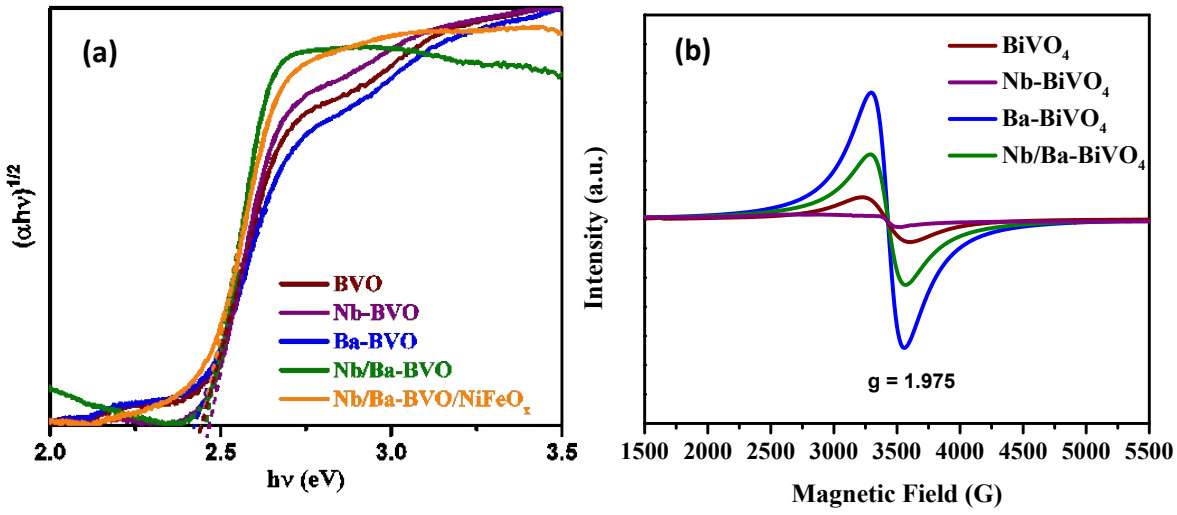

Fig. S6. (a) Tauc plot of $BiVO_4$ photoanodes for bandgap calculation. (b) EPR spectra of pristine, Nb-doped, Ba-doped, and Nb/Ba co-doped $BiVO_4$ films showing a V^{4+} resonance signal at g ≈ 1.975.

Optimization of the Synthesis Strategy. The successful co-doping of niobium and barium into the nanoporous $BiVO_4$ framework required a systematic optimization of the synthesis protocol to overcome fundamental chemical and physical barriers, as illustrated in Fig. S7. Our initial approach involved a mixed precursor strategy, where solutions of $NbCl_5$, $BaCl_2 \cdot 2H_2O$, and $(VO(acac)_2)$ in DMSO were simultaneously deposited onto the BiOI template (Fig. S7a). This method failed to improve performance (Fig. S7d), which can be attributed to two primary factors. First, the high reactivity of the V^{4+} species in the $VO(acac)_2$ solution likely leads to a rapid conversion of the BiOI template to $BiVO_4$, occurring before the Nb^{5+} and Ba^{2+} ions can be incorporated. Secondly, the higher ionic radii of Nb^{5+} and Ba^{2+} than V^{5+} lead to high diffusion of V^{5+} and its substitution into the lattice.

To decouple these competing reactions, a semi-sequential approach was attempted, wherein a $BaCl_2$ solution was first deposited and thermally treated at 200 ˚C for one hour, followed by a mixed solution of $NbCl_5$ and $VO(acac)_2$ (Fig. S7b). This experiment provided a key insight: while the first step successfully incorporated Ba, the subsequent co-deposition of Nb and V failed to incorporate niobium, resulting in performance identical to that of singly-doped Ba-$BiVO_4$ (Fig. S7e). The failure of this second step is again due to the aggressive reactivity of V^{4+}, which outcompetes the $NbCl_5$ for reaction with the now Ba-doped BiOI template, effectively locking out the Nb dopant.

These findings established that both dopants must be incorporated into the BiOI template before the introduction of the vanadium precursor. This led to our final, fully sequential deposition strategy (Fig. S7c). The optimized process addresses both the chemical reactivity and the desired spatial distribution of the dopants. By depositing and annealing $NbCl_5$ first,

the donor dopant is positioned deeper within the film near the FTO substrate, which is advantageous for improving charge transport and collection. The subsequent deposition and annealing of $BaCl_2$ places the acceptor dopant nearer the surface, where it can be more effective at passivating surface states or improving the interface for catalysis. Finally, the introduction of the $VO(acac)_2$ solution converts the stable, Ba- and Nb-co-doped BiOI template into the final photoanode. This strategy, which accounts for precursor reactivity and strategically places the dopants, is solely responsible for the dramatic synergistic enhancement observed in the photocurrent density (Fig. S7f). This behavior is attributed to the strong and rapid interaction of vanadium species with the BiOI framework during conversion, which can restrict dopant penetration in the mixed route, whereas stepwise thermalization in the sequential route promotes improved dopant anchoring prior to conversion.

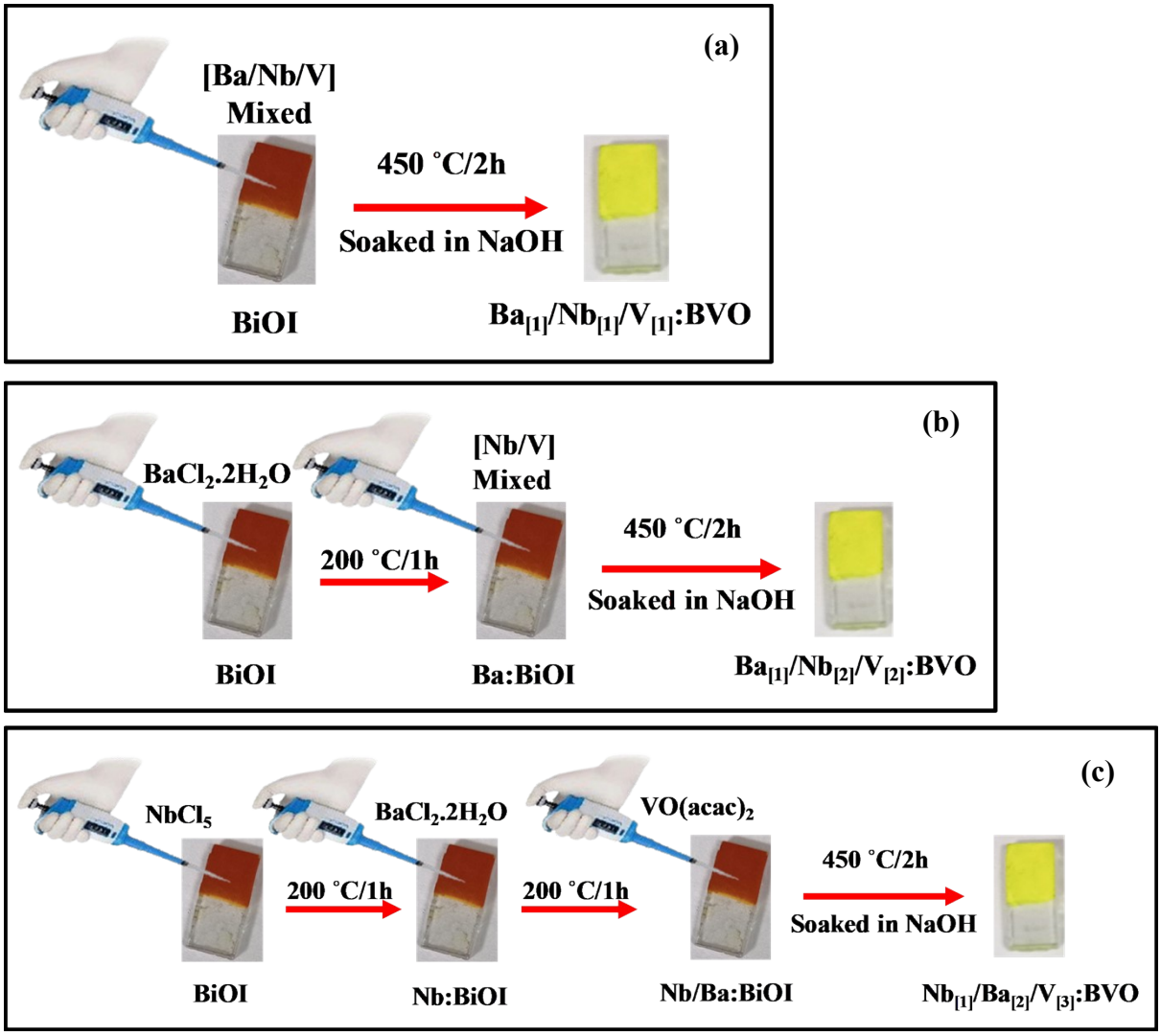

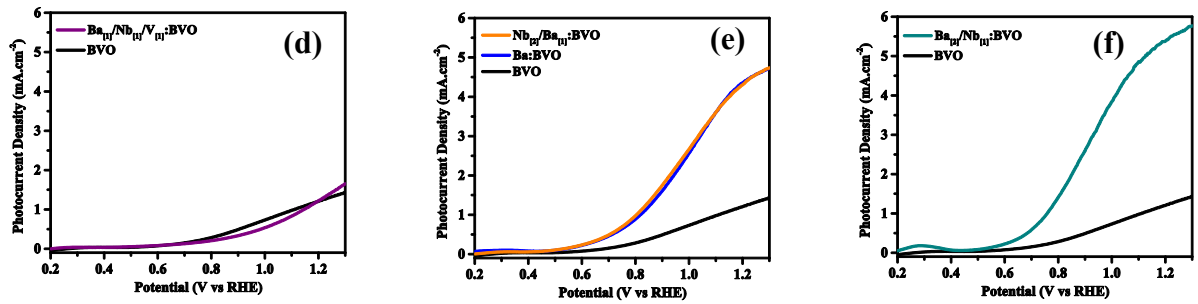

Fig. S7. Optimization of the sequential doping strategy for Nb and Ba incorporation. Synthesis schematics and corresponding photoelectrochemical performance. (a) Mixed precursor synthesis route. (b) Semi-sequential synthesis route. (c) Fully sequential synthesis route. (d-f) Linear sweep voltammograms (LSV) corresponding to the synthesis routes in (a-c).

Table S2. Nb/Ba–$BiVO_4$ photoanode performance compared with pristine, single-doped, and literature state-of-the-art $BiVO_4$ photoanodes prepared by the BiOI conversion method.

Photoanode	**Fabrication route**	**Photocurrent density at 1.23 V vs RHE (mA cm^{-2})**	**Ref.**
FTO/Nb/Ba–$BiVO_4$/$NiFeO_x$	BiOI → $BiVO_4$ sequential co-doping	6.2	This work
Nb/Ba–$BiVO_4$	BiOI → $BiVO_4$ sequential co-doping	5.5	This work
Ba–$BiVO_4$	BiOI → $BiVO_4$ sequential doping	4.5	This work
Nb–$BiVO_4$	BiOI → $BiVO_4$ sequential doping	3.2	This work
Pristine porous $BiVO_4$	BiOI → $BiVO_4$	1.5	This work
Nb/Ba–$BiVO_4$	BiOI → $BiVO_4$ Nb/Ba mixed in $VO(acac)_2$ DMSO	1.6	This work
FTO/SnO_2/Ba:$BiVO_4$/HfO_2/NiPt	BiOI → $BiVO_4$	6.5	1
Ba:$BiVO_4$	BiOI → $BiVO_4$	2.1	1
Fe-N-$BiVO_4$	BiOI → $BiVO_4$	5.7	2
Mo-$BiVO_4$/TiO_2/FeOOH	BiOI → $BiVO_4$	0.87	3
$BiVO_4$/Mo:$BiVO_4$/CoPi	BiOI → $BiVO_4$	5.10	4
W-$BiVO_4$/CoOOH	BiOI → $BiVO_4$	3.75	5
P-$BiVO_4$/$BiVO_4$	BiOI → $BiVO_4$	3.67	6
La/Co:$BiVO_4$	BiOI → $BiVO_4$	3.65	7
C-BVO/Co-FeOOH	BiOI → $BiVO_4$	5.08	8
B–Co:$BiVO_4$	BiOI → $BiVO_4$	2.27	9
$BiVO_4$/FeOOH/NiOOH	BiOI → $BiVO_4$	4.45	10

Reference

1. M. Arunachalam, K. S. Lee, K. Zhu and S. H. Kang, Adv. Energy Mater., **2024**, 14, 2402607.
2. J. Yang, C. Deng, Y. Lei, M. Duan, Y. Yang, X. Chen, S. Yang, J. Li, H. Sheng, W. Shi, C. Chen and J. Zhao, *Angew. Chem. Int. Ed.*, **2025**, *64*, e202416340
3. S. R. Sitaaraman, A. N. Grace and R. Sellappan, *RSC Adv.*, **2022**, *12*, 31380–31391
4. N. Wang, Y. Zhang, X. Xu, M. An, J. Gu, W. Song, J. Wan and L. Wang, *J. Alloys Compd.*, **2024**, *988*, 174274
5. Y. Sun, R. Tian, Y. Sun, J. Wang, W. Zhang, H. Cheng and Y. Liu, *ACS Appl. Mater. Interfaces*, **2025**, *17*, 18522–18534.
6. D. Xu, N. Gao, Q. Liu, X. Gao, Z. Chen and W. Shi, *Chem. Eng. Sci.*, **2026**, *321*, 122933.
7. H. Geng, S. Huang, D. Kong, E. Chubenko, V. Bondarenko, P. Ying, Y. Sui, Y. Zhao and X. Gu, J. Alloys Compd., **2022**, 925, 166667.
8. L. Yu, N. Chen, C. Liu, K. Xue, H. Luo, Z. Li, Y. Zhang and H. Zhu, Renewable Energy, **2026**, 256, 124223.
9. M. T. Naing, J. B. Hwang, J. Lee, Y. Kim, Y. Jung and S. Lee, Int. J. Hydrogen Energy, **2024**, 55, 234–242.
10. T. W. Kim and K. S. Choi, Science, **2014**, 343, 990–994.